JOURNAL OF SPACECRAFT AND ROCKETS
Vol. 36, No. 4, July–August 1999

Viscous Multiblock Simulations of Axisymmetric Launch Vehicle Flows

João L. F. Azevedo*
Instituto de Aeronáutica e Espaço, 12228-904 São José dos Campos, Brazil
Daniel Strauss†
Instituto Tecnológico de Aeronáutica, 12228-900 São José dos Campos, Brazil
and
Marcello A. S. Ferrari‡
Instituto de Aeronáutica e Espaço, 12228-904 São José dos Campos, Brazil

Axisymmetric, turbulent, viscous flow simulations over the first Brazilian satellite launcher are presented. The emphasis of the work is on multiblock calculations for afterbody flows. The multiblock capability is implemented over an existing thin-layer Navier–Stokes code, and results with both the Baldwin and Lomax and the Baldwin and Barth turbulence closure models are discussed. The details of the multiblock implementation are presented together with a brief description of the numerical method, based on the Beam and Warming implicit approximate factorization algorithm. The implementation is validated against previous solutions for forebody flows over the same vehicle and through comparisons with experimental data for afterbody flows. The increased resolution of the multiblock calculations for the afterbody region is evidenced through comparisons with previous single-block grid solutions.

Nomenclature

Cp = pressure coefficient
D = vehicle afterbody diameter
$\bar{E}$ = inviscid flux vector in the ξ direction
$\bar{F}$ = inviscid flux vector in the η direction
$\bar{H}$ = axisymmetric source term in general curvilinear coordinates
L = total body length
ℓ = reference length
M = Mach number
p = pressure
$\bar{Q}$ = vector of conserved variables in generalized curvilinear coordinates
q = magnitude of velocity vector
Re = Reynolds number
$\bar{S}$ = thin layer viscous flux vector in the η direction
t = time (Cartesian coordinate system)
x, y = Cartesian coordinates
Δt = time step
μ = molecular viscosity coefficient
ξ, η = generalized curvilinear coordinates
ρ = density
τ = time (generalized curvilinear coordinate system)

Subscripts

jet = rocket nozzle jet quantities
∞ = freestream quantities

Introduction

ONE of the largest aerospace projects under development in Brazil at the moment concerns the first Brazilian satellite launch vehicle (VLS). This vehicle is a four-stage launcher for small, low-Earth-orbit payloads. For several reasons, inherent to the Brazilian lack of availability of suitable wind-tunnel test facilities, the use of computational fluid dynamics techniques has become over the years an essential part of the aerodynamic analysis and design of the VLS. In this context, a fair amount of work has been devoted to the development of reliable computational tools for flow simulations relevant to the VLS aerodynamic design. The long-term goal of such work is the implementation of the capability of simulating increasingly complex flows, either from a geometric or a physical point of view.

The present work arose from the need to numerically investigate afterbody flows for the VLS system and, in particular, the interaction between the external flow and the plumes from the rocket motor nozzles. Because of the complexity of the geometry in the afterbody region, and with the objective of keeping the codes as modular as possible while still remaining with a structured grid approach, the decision was made to extend the existing capability[1,2] in the direction of implementing multiblock techniques. This capability included the possibility of accurately simulating turbulent viscous flows over axisymmetric launch vehicle configurations. Three eddy viscosity turbulence models were available, and fairly complex forebody flows have been studied in detail in the past.[2]

Several aspects come into play when one considers afterbody flows. Actually, for the present axisymmetric case, the complexity of the geometry is not as overwhelming an issue as it could be for realistic three-dimensional cases. Therefore, one could probably deal with the present problem using a single-block grid. However, in the present context, there was interest in developing tools that could be used as building blocks to handle even more complicated configurations in the future. Based on the group's previous experience, it seemed that the best approach would be to use block structured grids. The basic ideas underlying the present development were that each block should be able to internally identify the types of boundaries on its four sides and that each side should consist of one single type of boundary. The first requirement makes the code implementation modular in the sense that there are no specific tests for any particular block, whereas the second one greatly simplifies the implementation of boundary conditions and turbulence models. For ease of implementation, patched multiblock grids have been used at the present stage in this development.

Therefore, the work describes the general ideas of the multiblock extension, with applications to forebody flow cases for which results were previously available with a single-block formulation.[2]

Received 24 January 1998; revision received 8 November 1998; accepted for publication 10 November 1998. Copyright © 1999 by the authors. Published by the American Institute of Aeronautics and Astronautics, Inc., with permission.

*Head, Aeroelasticity and Computational Fluid Dynamics Sections. Senior Member AIAA.

†Undergraduate Student, Department of Aeronautical Engineering.

‡Assistant Research Engineer, Computational Fluid Dynamics Section; currently Product Development Engineer, Aerodynamics Section, EMBRAER, DTE/GEA/EAD, 12227-901 São José dos Campos, Brazil.

After this initial validation, the code is applied to afterbody flow simulation cases. Major emphasis of the present work is on afterbody cases without a propulsive jet, but some results with the presence of nozzle jets are also included. Clearly, the long-term objective of the development is to create the ability to include jets at realistic pressure and temperature ratios. The flowfields over the VLS at zero angle of attack are modeled by the axisymmetric thin-layer Navier–Stokes equations.[3–5] Three different models are available for turbulence closure, namely, the Baldwin and Lomax[6] algebraic model, the Johnson and King[7] half-equation model, and the Baldwin and Barth[8] one-equation model. However, all of the results here reported have used either the Baldwin and Lomax[6] or the Baldwin and Barth[8] models. For some of the flow cases of interest, the Baldwin and Lomax[6] model is clearly not an ideal choice. Nevertheless, there was an attempt to use this model in the initial validation phase due to its simplicity. The calculations, however, indicated that a more robust model was necessary, and the best results obtained for the afterbody flows have used the Baldwin and Barth[8] model.

Within each block, the governing equations were discretized using the standard Beam and Warming implicit approximate factorization algorithm.[9,10] The implicit Euler method is adopted for the time march and three-point, second-order central difference approximations are used for the spatial derivatives. Artificial dissipation terms are explicitly added to maintain numerical stability. All computations reported in the present work have used a nonlinear artificial dissipation model.[11] The forthcoming sections describe the theoretical formulation and numerical method, with emphasis on the details of the multiblock implementation. The computational results are presented together with their discussion and comparison with available data.

Theoretical Formulation

The first Brazilian VLS is of the cluster type with four strap-on boosters around the central core. This vehicle has a hammerhead-type fairing, which is a somewhat common configuration for satellite launchers to accommodate spacecraft with a diameter larger than the last boosting stage. Further description of this vehicle can be seen, for instance, in Ref. 12. The flowfield over the complete VLS vehicle, even at zero angle of attack, is certainly three dimensional. The effect of the four strap-on boosters, however, will not be considered in the present work, and only the geometrically axisymmetric central body is included in the simulations.

The azimuthal-invariant, Reynolds-averaged, thin-layer Navier–Stokes equations[3,4] can be written for the case of no body rotation in general curvilinear coordinates as

$$\frac{\partial \bar{Q}}{\partial \tau} + \frac{\partial \bar{E}}{\partial \xi} + \frac{\partial \bar{F}}{\partial \eta} + \bar{H} = \frac{M_\infty}{Re}\frac{\partial \bar{S}}{\partial \eta} \tag{1}$$

A suitable nondimensionalization of the governing equations is assumed to write Eq. (1). In the present case, the choice of reference state proposed in Ref. 10 is adopted. The form of the earlier defined algebraic vectors can be found, for example, in Refs. 5 and 13. In Eq. (1), M_∞ is the freestream Mach number and the Reynolds number is defined in its usual form as

$$Re = \frac{\ell \rho_\infty q_\infty}{\mu_\infty} \tag{2}$$

Expressions for the required metric terms and for the Jacobian of the coordinate transformation can be found in Refs. 4 and 13, among other references.

The correct account for the viscous effects in the present case involves the implementation of an appropriate turbulence closure model. Three different eddy viscosity models were available in the single block code.[2] These were the Baldwin and Lomax algebraic model,[6] the Johnson and King half-equation model,[7] and the Baldwin and Barth one-equation model.[8] For a complete description of each of these models, the interested reader is referred to the original references already cited. Here, the authors will concentrate on the aspects that are specific for the present applications.

The implementation of the Baldwin and Lomax model[6] adopted in the present case is a straightforward extension to the axisymmetric case of the work of Menezes.[14] The equations for the model are the ones widely available in the literature except that, to be consistent with the present nondimensionalization, the eddy viscosity expressions are multiplied by a factor Re/M_∞. The expressions for the model are implemented in terms of the dimensionless variables and, in general, curvilinear coordinates, following the work presented in Ref. 15. Moreover, the model is modified in wake regions as suggested in Ref. 4.

The Baldwin and Barth model[8] is a one-equation model that attempts to avoid the need to compute algebraic length scales, without having to resort to more complex two-equation- or k–ϵ-type models. The model was implemented in the present code precisely as described in Baldwin and Barth's original work.[8] The extension of the model for compressible flows was obtained simply by multiplying the kinematic turbulent viscosity coefficient by the local density, as also indicated in Ref. 8. Moreover, the turbulence model equation is solved separately from the other governing equations in a loosely coupled fashion. This procedure was adopted to avoid having to modify the flux Jacobian matrices and the overall structure of the flow solution algorithm, which had been previously implemented.

Numerical Implementation

Spatial and Temporal Discretization

The governing equations were discretized in a finite difference context on a structured quadrilateral mesh that would conform to the body. The computational mesh could be formed by as many patched blocks as necessary to discretize the geometry. The mesh generation within each block could, in principle, be performed in a completely independent fashion. However, for all cases studied in the present work, there was a definite attempt to guarantee some continuity of the mesh spacing across contiguous blocks. Moreover, the block division is such that each side of a block has a single type of boundary condition.

The Beam and Warming implicit approximate factorization scheme[9,10] was used, with the implicit Euler method selected for the time march. As usual with the Beam and Warming algorithm, the spatial derivatives were centrally differenced using three-point, second-order finite difference operators. Discretization of the viscous terms uses the so-called midpoint operators to obtain a compact finite difference stencil at each point and to avoid the need for a different discretization of these terms close to block computational boundaries. Artificial dissipation terms were added to the formulation to control nonlinear instabilities. All results reported in the present work have used Pulliam's nonlinear artificial dissipation model.[11] Implicit artificial dissipation terms were implemented as described in Refs. 16 and 17.

The axisymmetric source term was treated fully explicitly in the present case. Numerical experiments indicated that the implicit implementation of this term had a significant detrimental effect on the convergence characteristics of the method. Variable time stepping was used to accelerate convergence to steady state. The implementation of the variable time-step option, or constant Courant–Friedrichs–Lewy (CFL) option, also follows the work in Refs. 16 and 17. All boundary conditions were treated explicitly in the cases analyzed, including boundaries between computational blocks.

For the axisymmetric simulations, the types of boundary conditions that should be considered include solid wall, centerline or symmetry, far-field, (downstream) exit plane, jet exit, and block interface boundary conditions. Wall boundary conditions are obtained by imposing no slip at the wall and zero normal pressure gradient and by assuming the wall to be adiabatic. The centerline, both upstream and downstream of the body, is a singularity of the coordinate transformation in the axisymmetric case. Hence, the governing equations are never solved at the centerline itself. The present approach considers a line of computational points on the other side of the centerline to impose symmetry boundary conditions along this line.

Far-field conditions simply assume freestream values can be specified at this computational boundary. This is possible in the present case because the far-field boundary is typically located fairly far away from the body. Downstream conditions are based on the concept of one-dimensional characteristic relations[16] to determine the number of variables that should be extrapolated at this boundary. For a subsonic downstream boundary, the static pressure is fixed and all other quantities at the boundary are obtained by zeroth-order extrapolation of their respective values in the adjacent interior point. All flow variables are extrapolated from the adjacent interior point for a supersonic outflow. The jet boundary conditions follow the same reasoning based on characteristic relations. From the point of view of the present computational domain, the jet is seen as a supersonic entrance[17] because only sonic and supersonic jets were considered in this work. Therefore, all jet properties are specified at this type of boundary. The treatment of block interfaces will be discussed in the next section.

Multiblock Implementation

An initial attempt to treat afterbody flows over the VLS is described in Ref. 18. This work used the available forebody flow simulation codes[1] and extended the computational mesh to also include the afterbody region. However, in an attempt to continue to use the available single-block approach, the meshes had a half-O type of topology. Although results with and without jets have been computed and are shown in Ref. 18, the quality of the solutions clearly reflects the lack of adequate resolution in the wake region of the flow. These results, although qualitatively correct, do not contain all of the phenomena that should be present in the body wake or in the jet mixing layer.

The use of multiblock grids, however, allow for a much greater control of grid refinement in the regions of interest, and this can be accomplished without having to increase the number of grid points in regions where there is no need for such refinement. Therefore, one can improve the solution quality without excessive computational cost penalties. Moreover, a multiblock approach alleviates the burden of generating structured meshes over very complex configurations. In the present case, for instance, the future addition of the rocket nozzles in the complete configuration would be very difficult without such capability.

A patched multiblock approach has been adopted in this first stage of the capability implementation. The basic ideas underlying the present development were that each block should be able to internally identify the types of boundaries on its four sides and that each side should consist of one single type of boundary. Another basic assumption in the present development was that the solution procedure within each block should be implemented in a completely independent fashion. Therefore, additional details of a given configuration could be added on to the simulation simply by creating new grid blocks that would describe such features. The code was constructed such that the current block (being operated on) responds as if it is the only block in the mesh.

Each computational block has information of the types of boundaries in its four sides. As already indicated, each side of the block has one single boundary type for all of the points in that side. Therefore, the block is operated on using the described algorithm and the boundary conditions indicated for its sides. These block boundary conditions are specified through the input file using flags, which identify the boundary condition type for each block side. The various types of boundary conditions have also been discussed, except for the internal boundaries between blocks. In this case, the mesh is generated such that there is an overlap of two grid points between the adjacent blocks, as indicated in Fig. 1.

The present code only applies the described algorithm for interior grid points. Boundary points are always updated through boundary conditions. Hence, with the grid overlap arrangement shown in Fig. 1, the block interfaces are perceived by the block currently being operated as boundaries with Dirichlet-type boundary conditions. The first overlapped point is an interior point of the block being operated. Therefore, the governing equations are solved at this point. The second overlapped point is the actual boundary point of the current block, and its property values are not changed during the current block solution. It should be noted that this second point is an interior point for the other block. Its properties are, therefore, updated through the actual solution of the governing equations when the other block is operated on. After the solution within the block is completed, the information on the first overlapped point is passed on to the neighboring blocks such that their boundary information is updated. This treatment of block interfaces amounts to an explicit enforcement of boundary conditions across the blocks.

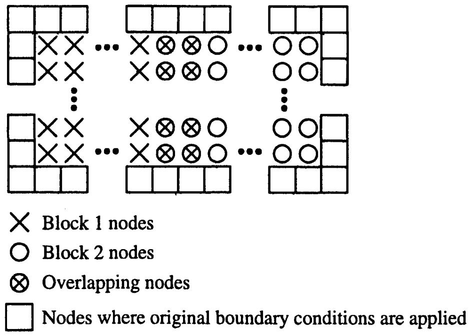

Fig. 1 Indication of the communication of information between grid blocks.

Grid Generation

The computational meshes used were all generated by algebraic methods within each block. In particular, the multisurface algebraic grid generation technique described by Fletcher[19] has been implemented in a fairly general code for the present configurations. The code allows for grid clustering at various regions along the longitudinal direction, as well as for a large amount of control in the grid point distribution along the normal direction. Both hyperbolic tangent and exponential grid stretching functions are used to obtain the desired grid clustering and coarsening over the body.

In the forebody region, the objective was to concentrate grid points in the longitudinal direction around expansion corners and in regions of expected shock impingement and/or flow separation. In the afterbody region, points were concentrated toward the vehicle base in the longitudinal direction and along the mixing layer region between the external and the base flow in the nominally normal direction. In particular, there was a clear attempt to enforce some continuity of the mesh spacing distribution across contiguous blocks to avoid numerical errors due to sudden changes in the grid spacing. Nevertheless, it is not always possible to obtain a complete matching of all grid spacings involved.

The grid generator also guarantees mesh orthogonality at least in the proximity of the body wall. The user can specify the distance normal to the wall until which grid orthogonality is forced. The compromise in this case is associated with avoiding mesh line crossings as the grid is refined in the longitudinal direction. The longer the distance of forced orthogonality normal to the wall, the harder it is to avoid such crossings. The mesh generator also allows for the control of the value of y^+ for the first grid point off the wall, which is a parameter typically associated with the suitability of a grid for viscous turbulent calculations.

Results and Discussion

The first tests performed with the multiblock capability were an attempt to reproduce results that were previously calculated[2] with the single-block code, to validate the present implementation. These are results for the forebody portion of the vehicle and the single-block grid used in these calculations is shown in Fig. 2. This particular grid has 156 × 65 points in the longitudinal and nominally normal directions, respectively, and a value y^+ of approximately 3 for the first grid point off the wall. All forebody computations presented here used the Baldwin and Lomax[6] algebraic eddy viscosity model.

Multiblock computations have been performed for this configuration using two blocks and using four blocks. The four-block results will be presented here. The computational mesh for this case is shown in Fig. 3. This mesh is essentially equivalent to the one presented in Fig. 2, except that it is topologically divided into four blocks. Figure 3 shows these blocks separated solely to facilitate the reader's understanding of the block breakup. Simulations for freestream Mach numbers of 0.5 and 0.73 were performed with the four-block grid. Results for the $M_\infty = 0.73$ case are shown in Fig. 4 in terms of pressure contours. The Reynolds number for this calculation was 20×10^6, based on the afterbody diameter. One can observe from Fig. 4 that there is very good continuity of pressure contour lines across block interfaces. Incidentally, the block interfaces with their two overlapped points are also indicated in Fig. 4. The good continuity characteristics of the property contour lines across block interfaces is an indication of the correction and efficiency of the communication between computational blocks.

The pressure coefficient distributions along the body for this case are shown in Fig. 5. Figure 5 compares the current multiblock solution with the single-block solution reported in Ref. 2. One can observe a very good agreement between the two results, indicating that the multiblock calculation is as good as the previous single-block result. Moreover, at least for this case, these results indicate that the need to pass information across blocks has not caused any deterioration in the numerical solution. Moreover, the convergence rate of the multiblock solution is completely equivalent to that observed with the single-block case. This can be clearly seen from Fig. 6, which shows the convergence history for the $M_\infty = 0.73$ case with single- and with multiple-block grids. Both computations were run with the same CFL number, using the variable time-step option described earlier. The results in Fig. 6 indicate that the explicit treatment of the internal boundary conditions are not reducing the rate of convergence to steady state in this case. Furthermore, this is an indication that the present multiblock implementation does not cause any degradation in the level of solution convergence possible with the algorithm.

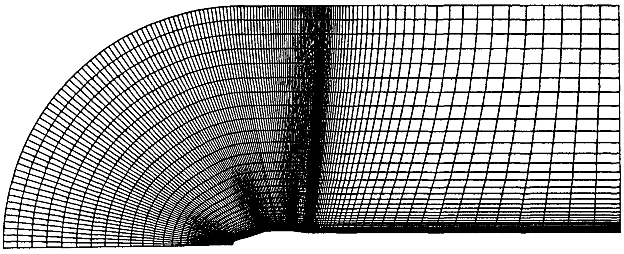

Fig. 2 Single-block computational mesh for vehicle forebody used to provide results for validation.

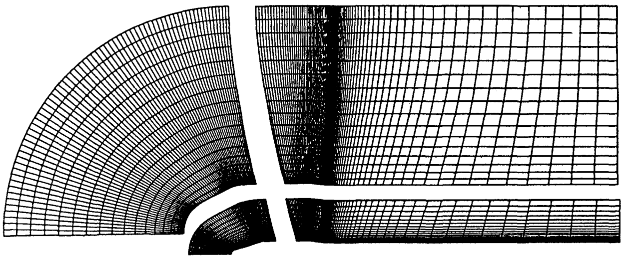

Fig. 3 Four-block grid for the VLS forebody.

The preceding results provided confidence in the correct implementation of the multiblock procedure in the present case. Therefore, the forthcoming tests will consider the afterbody flows that are the major motivation for the present work. The initial comparison is performed with some of the results available in Ref. 18, which was a previous attempt to simulate afterbody flows for the VLS, as already described. The first simulated case considers freestream flow with $M_\infty = 0.5$, $Re = 20 \times 10^6$, and no rocket jets in the vehicle base. In other words, there is simply a base in the back of the vehicle. The computational mesh used in the simulations of Ref. 18 is shown in Fig. 7, whereas the present multiblock mesh is shown in Fig. 8. Note that the computations being here attributed to Ref. 18 are actually calculations performed by the present authors using the codes and computational meshes developed by the author of the cited reference. The results are, however, completely equivalent to those presented in Ref. 18. Moreover, the mesh shown in Fig. 8 has three computational blocks. The first block comprises the complete vehicle up to the base, and it is somewhat equivalent to the mesh shown in Fig. 2, except for some additional grid clustering in the longitudinal direction as the base region is approached. The second block includes the region from the vehicle base until the downstream boundary, with a height equal to the base height. The third block completes the computational domain in this case.

A comparison of the results obtained with the two different approaches can be seen in Figs. 9. Figures 9 show pressure contours in the base and near wake regions. The block interface lines are also shown in Figs. 9 for the multiblock cases. Figure 9a presents the results obtained with the single-block, O-type mesh shown in Fig. 7. This was calculated with the Baldwin and Lomax turbulence closure model. Figure 9b presents the results obtained with the three-block mesh shown in Fig. 8 also using the Baldwin and Lomax model. As mentioned, block division lines are shown in Figs. 9, and these give an idea of the continuity of pressure contours across the interfaces. In general, for the afterbody results with the Baldwin and Lomax model, continuity is very good in regions of high mesh density. However, it is also evident that, farther downstream of the vehicle base, the continuity of pressure contours is not as good. Nevertheless, the multiblock calculation yields an increased resolution of the flow features in the vicinity of the vehicle base. Moreover, these results seem to correct the anomalous behavior in the pressure contours observed for the single-block solution in the vicinity of the downstream centerline.

In an attempt to improve the contour continuity across block interfaces, the same physical problem was solved using the multiblock code with the Baldwin and Barth turbulence closure model. The results are presented in Fig. 9c. Clearly, there is good continuity of pressure contour lines throughout the near-wake region for this case. Generally, the Baldwin and Barth solution is fairly different from the other two. In particular, the results shown in Figs. 9b and 9c use exactly the same computational mesh, and the solution is quite

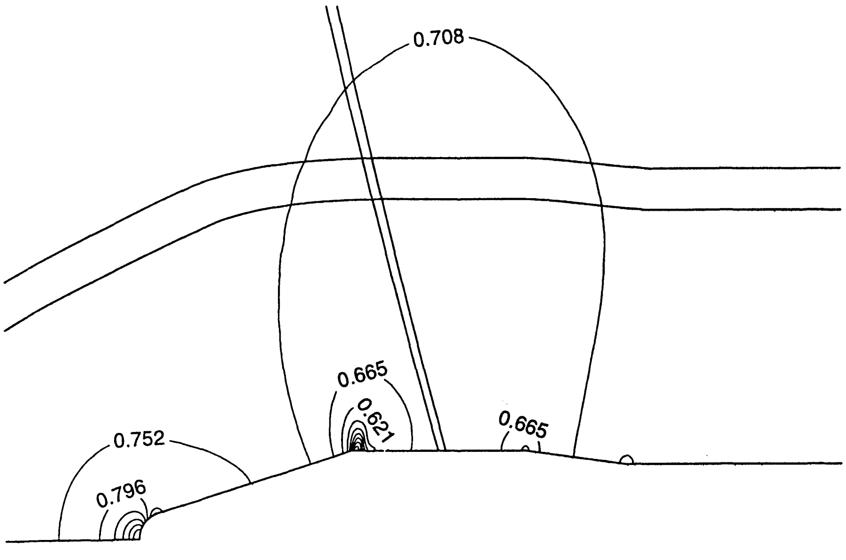

Fig. 4 Pressure contours over the VLS forebody for $M_\infty = 0.73$; four-block grid, also showing block interface lines.

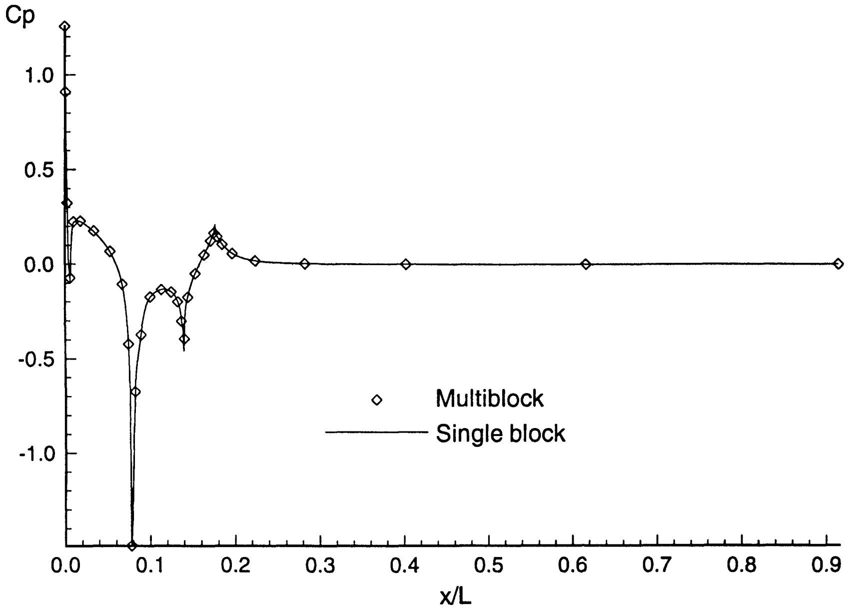

Fig. 5 Comparison of single-block and multiblock pressure coefficient distributions along the body for $M_\infty = 0.73$ and $Re = 20 \times 10^6$.

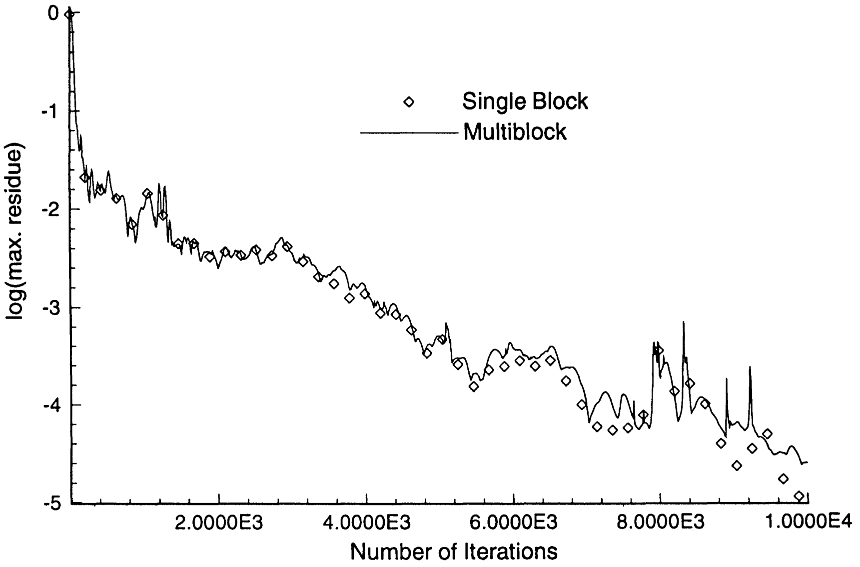

Fig. 6 Comparison of single-block and multiblock convergence histories: $M_\infty = 0.73$ and $Re = 20 \times 10^6$.

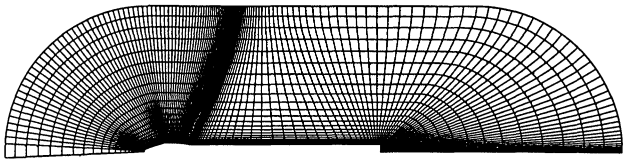

Fig. 7 Single-block grid including the afterbody region.

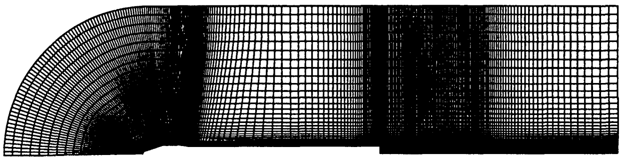

Fig. 8 Typical multiblock grid used for the afterbody flow simulations.

different. On the other hand, the two calculations with the Baldwin and Lomax model, although using very different meshes, have a somewhat similar pattern for the pressure contour plots. Moreover, one can clearly observe a backward motion of the rear stagnation point for the Baldwin and Barth solution, as compared to the other two earlier cases.

A more quantitative comparison of the rear stagnation point position for these three cases is presented in Table 1. Table 1 presents the axial position along the centerline of the rear stagnation point nondimensionalized by the afterbody diameter. The computational results are also compared in Table 1 with experimental data for cylindrical afterbodies obtained from Ref. 20. These results indicate that the numerical solution with the Baldwin and Barth model provides a better correlation with the experiment for this flow case. The authors of Ref. 20 indicate that the development of the near wake is dependent on the flow conditions approaching the separation point. Previous results^2 have indicated that, even for forebody flows, the Baldwin and Barth model provides a far more robust prediction of the boundary-layer behavior along the body. Therefore, one should indeed expect to obtain better results with the Baldwin and Barth model for the present afterbody cases, regardless of the added resolution that this model should provide at the base region itself.

Further comparison of the relative computational efficiency of the single-block and multiblock calculations can be seen in Fig. 10. Figure 10 presents the convergence history plots for the two cases in Figs. 9a and 9b, i.e., for the afterbody simulations using the Baldwin and Lomax turbulence closure model and using, respectively, the single-block grid of Fig. 7 and the three-block grid of Fig. 8. As before, there is apparently no convergence rate degradation in the multiblock solution as compared to the single-block case. However, the multiblock final residue is slightly higher than the one obtained in the other case. On the other hand, it should be observed that there was no attempt to drive the residues to machine zero in either case.

Several other cases were run for this all-base afterbody configuration. All of these cases used the Baldwin and Barth turbulence closure model[8] and assumed a Reynolds number of 20 x 10^6 based on the afterbody diameter. The parameter varied in these studies was the freestream Mach number. The dimensionless pressure contours in the near-wake region for some of these cases are shown in Fig. 11. In particular, Fig. 11 shows the results for $M_\infty = 0.73$, 0.80, and 0.94. The computational grid used for these calculations is the one shown in Fig. 8. A detail of the interface between blocks 1 and 3, indicated in the Fig. 11c, is shown in Fig. 12. The results reproduce the general trend of the expected behavior, and as before, the block interface lines are shown in Fig. 11 to indicate the good contour continuity across such interfaces.

It is interesting to observe that a first analysis of Fig. 11c, i.e., the one corresponding to the $M_\infty = 0.94$ case, would seem to indicate the existence of discontinuities in the contour lines across the interface between blocks 1 and 3. However, a closer look at this interface reveals that there are no such discontinuities. This can be verified considering the inset in Fig. 11 and the corresponding enlarged plot in Fig. 12. A similar behavior is observed for the other contour lines at this interface. The two vertical lines in Fig. 12 are exactly the block interface lines. Therefore, Fig. 12 is clearly indicating a very smooth crossing of the interface by the pressure contour lines. The computations for the $M_\infty = 0.94$ case were repeated using a grid that is identical to the one shown in Fig. 8, but is topologically formed as a single-block grid. The pressure contours obtained were identical to those shown in Figs. 11 and 12. The apparent break in the overall smoothness of the pressure contours near the body base for the $M_\infty = 0.94$ case seems to be associated with the rapid grid size variation in the region that, in turn, causes very different levels of artificial dissipation at neighboring points. In any event, the results indicate that the most important aspect here is that the communication of information across block boundaries is not causing any error. This is clearly demonstrated by Figs. 4, 5, 9, 11, and 12, where the latter explains the apparent anomalies observed in Fig. 11c for the $M_\infty = 0.94$ case.

Some validation of these afterbody simulations was obtained through comparisons of the rear stagnation point positions with experimental data. The data used was obtained from Ref. 20 for the subsonic freestream cases and from Ref. 21 for the supersonic case.

Table 1 Position of rear stagnation point behind body base for $M_\infty = 0.5$ and $Re = 20 \times 10^6$

Case description	Position, x/D
Computation, single-block, Baldwin–Lomax model	0.97
Computation, multiblock, Baldwin–Lomax model	0.82
Computation, multiblock, Baldwin–Barth model	1.35
Experimental data, Ref. 20	1.21

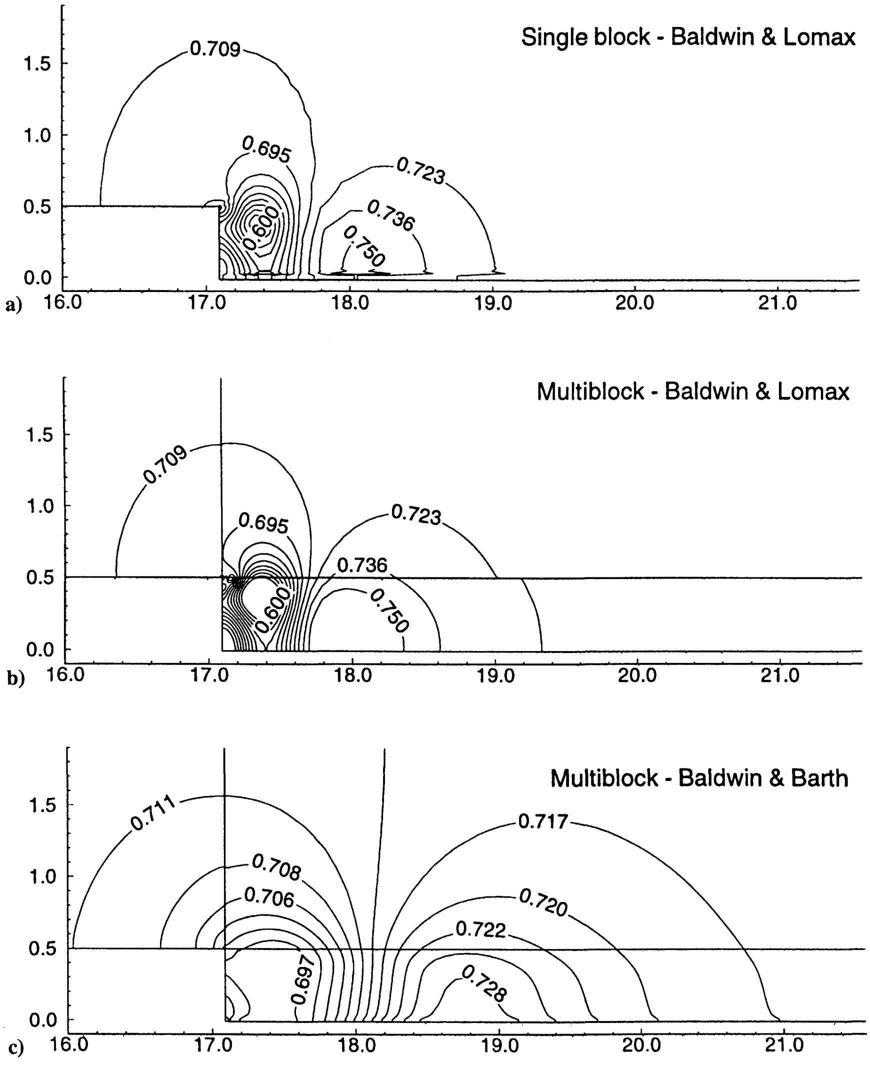

Fig. 9 Pressure contours in the base region for $M_\infty = 0.5$ and $Re = 20 \times 10^6$.

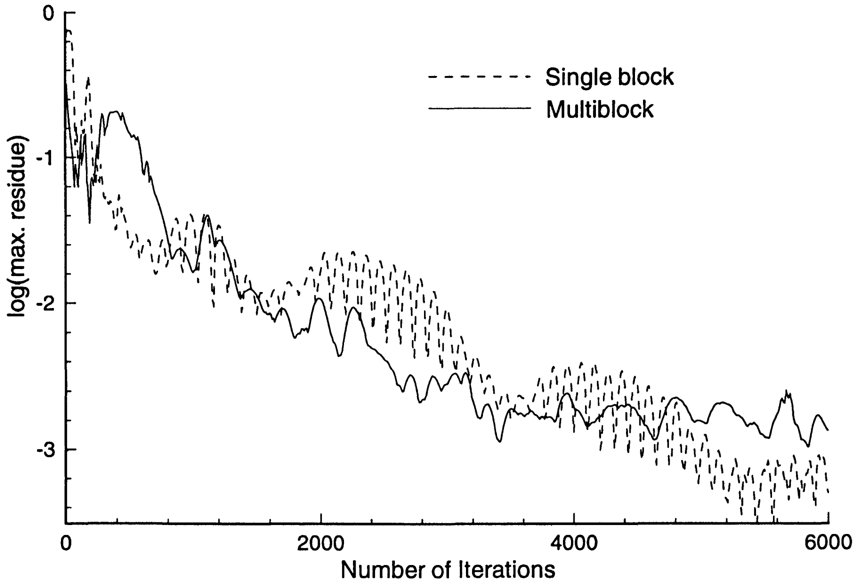

Fig. 10 Convergence histories for the all-base afterbody simulations with the Baldwin and Lomax turbulence closure model: $M_\infty = 0.5$ and $Re = 20 \times 10^6$.

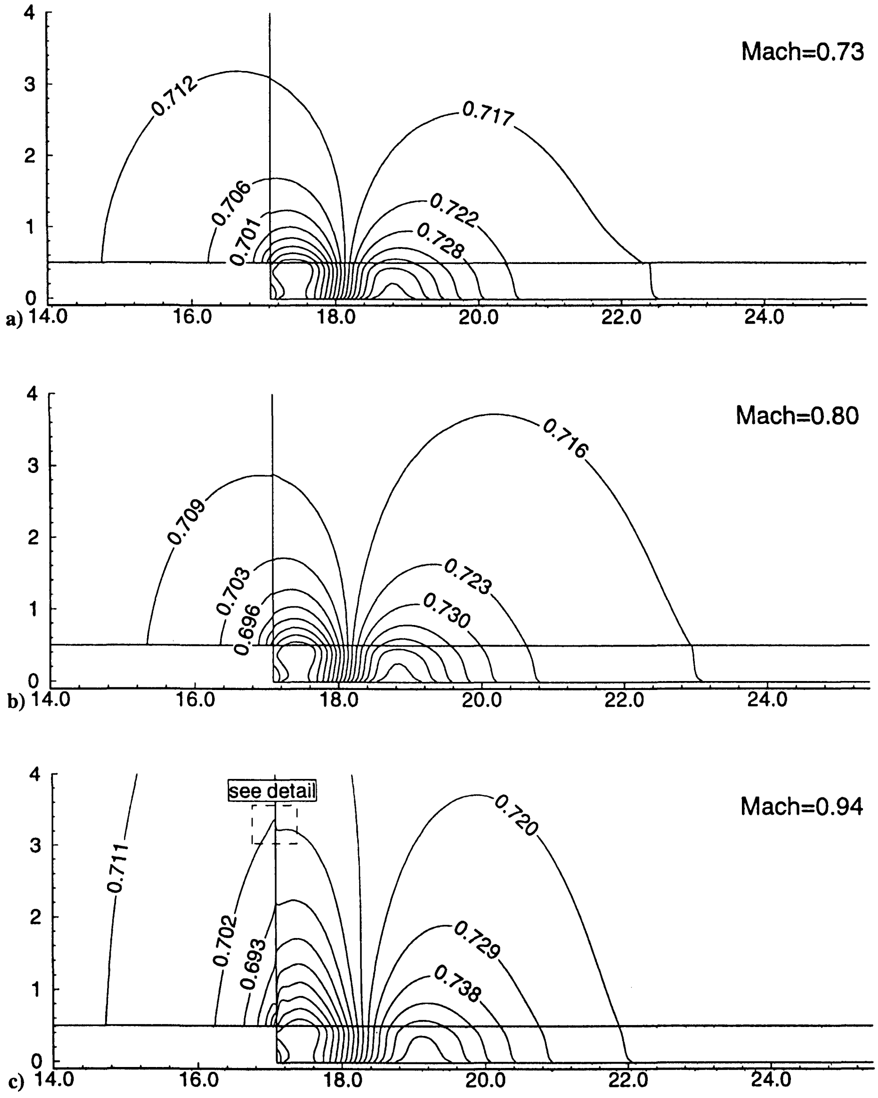

Fig. 11 Pressure contours in the base region for different Mach numbers and $Re = 20 \times 10^6$; all computations use the Baldwin and Barth model.

This comparison is presented in Table 2 in terms of the axial position along the centerline of the rear stagnation point, measured from the vehicle base and made dimensionless by the afterbody diameter. The errors in the prediction of the rear stagnation point position are at most of 10% in the subsonic freestream cases. This error, however, is higher for the supersonic case. In general, one observes that the rear stagnation point moves downstream as the Mach number is increased in the subsonic cases, which is the expected behavior according to Ref. 20. However, this movement is less pronounced in the computational results than in the actual experiments. Hence, for the lower Mach numbers, the computational stagnation points are farther downstream than the experimental results, whereas for the higher Mach numbers (in the subsonic regime) the opposite occurs.

The experimental result for the supersonic case comes from a different set of experimental data.[21] It is indicating a larger difference in the rear stagnation point position between computation and experiment. Furthermore, it continues the trend of having the experimental stagnation point located downstream of the computational one, which was already observed for the higher Mach number subsonic cases. Pressure contours for this supersonic case with freestream Mach number $M_\infty = 2.5$ are shown in Fig. 13. Figure 13 shows most of the complete computational domain, including the vehicle forebody. The more relevant features of this flowfield are evident from Fig. 13. Hence, both the detached bow shock and the oblique shock at the end of the payload boattail can be clearly seen. Similarly, the expansion at the corner of the base and the recompression in the near-wake region are also clearly identified Fig. 13. Moreover, the pressure contours do not present any indication of block interface influence in the results.

Table 2 Position of rear stagnation point behind body base; computations consider $Re = 20 \times 10^6$

Freestream Mach number M_∞	Computational x/D	Experimental x/D
0.50	1.35	1.21
0.73	1.41	1.39
0.80	1.43	1.47
0.94	1.59	1.76
2.50	0.94	1.32

As already stated, the major emphasis of the present work is on afterbody cases without a propulsive jet. However, the long-term objective of this development is obviously to create the capability of including in the simulation jets at realistic pressure and temperature ratios. To this end, a few preliminary cases with a propulsive jet were simulated. The authors emphasize, however, that these are initial results and that the cases with a propulsive jet have received far less attention so far than the discussed power-off base cases. The configuration considered in these studies is essentially identical to the earlier one, except that a rocket nozzle jet occupies the complete extension of the vehicle base. Therefore, the computational mesh used for the multiblock calculations is again the one shown in Fig. 8.

A representative result of the simulations with a base jet performed so far is presented in Fig. 14. The freestream conditions in this case are given by $M_\infty = 0.5$ and $Re = 20 \times 10^6$. The jet conditions consider $M_{\text{jet}} = 1.0$, $p_{\text{jet}} = 3p_\infty$, and $T_{\text{jet}} = 2T_\infty$. Moreover, it is assumed that the jet enters the computational domain parallel to the vehicle longitudinal axis. Mach number contours in the wake/plume region are shown in Fig. 14. Although Fig. 14 only shows the afterbody portion of the flow, it should be emphasized that the computation considers the complete vehicle as in the earlier cases. The structure of the flowfield in the vicinity of the jet

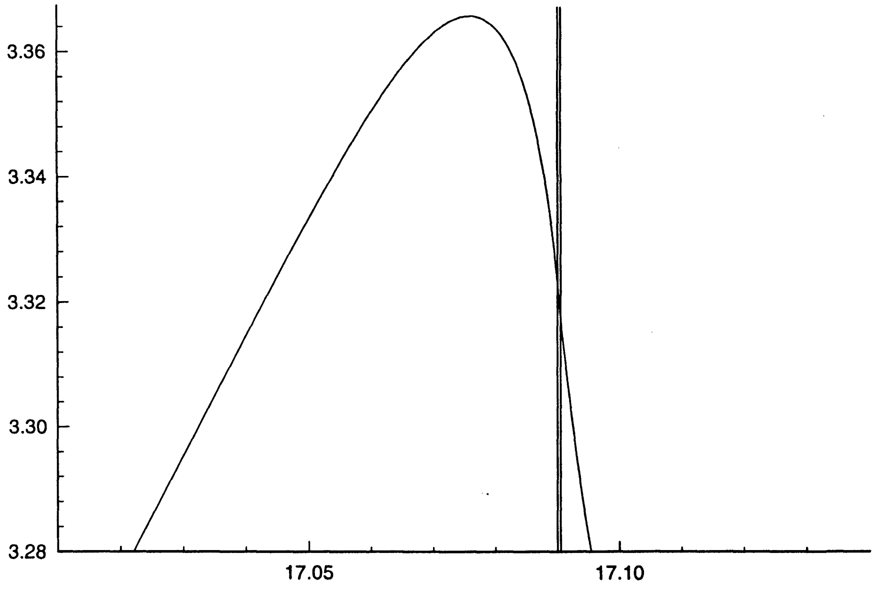

Fig. 12 Detail of the pressure contours for the $M_\infty = 0.94$ and $Re = 20 \times 10^6$ case in the vicinity of the interface between blocks 1 and 3.

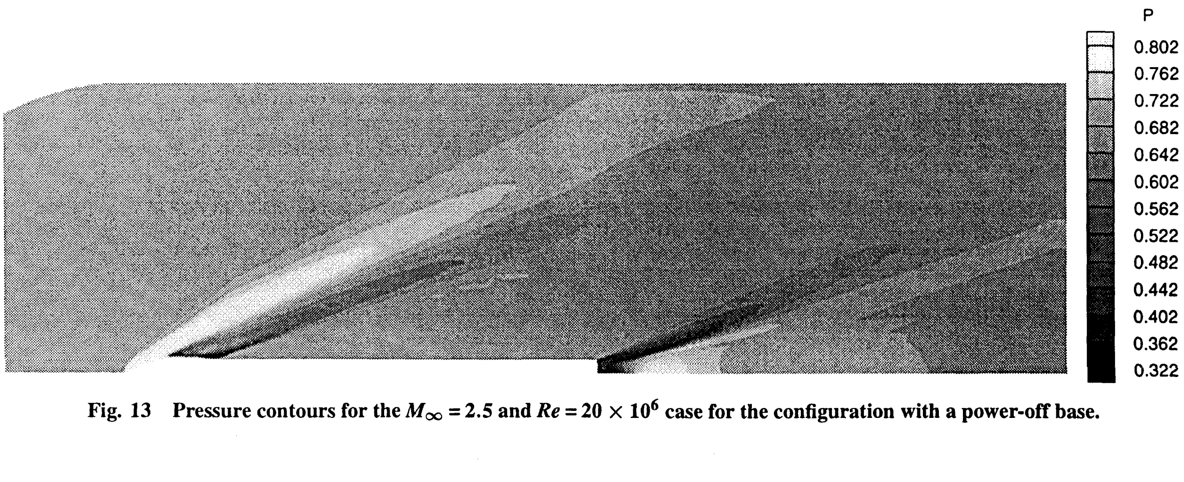

Fig. 13 Pressure contours for the $M_\infty = 2.5$ and $Re = 20 \times 10^6$ case for the configuration with a power-off base.

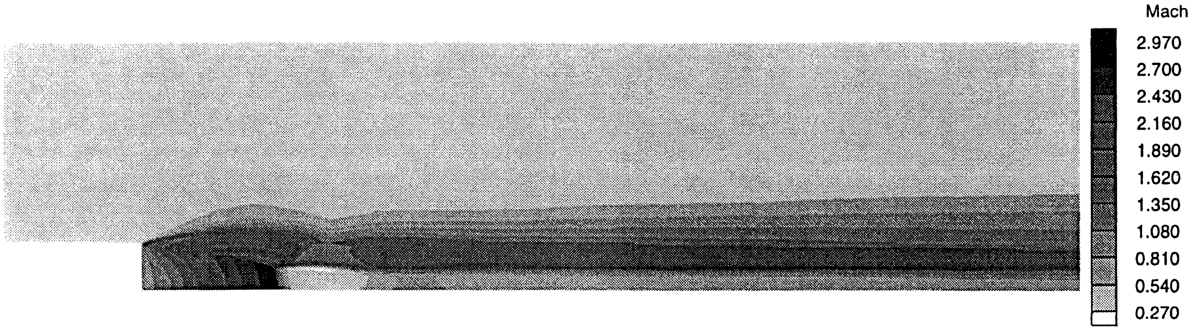

Fig. 14 Mach number contours in the wake/plume region for the case with a propulsive jet: $M_\infty = 0.5$, $Re = 20 \times 10^6$, $M_{jet} = 1.0$, $p_{jet} = 3p_\infty$, and $T_{jet} = 2T_\infty$.

exit is well defined, as one can see Fig. 14. Moreover, the overall features of the flow are in agreement with those observed in the results of Ref. 18. The basic difference is that, because Ref. 18 uses the single-block, O-type mesh shown in Fig. 7, the results in that reference already show the lack of grid resolution even at a short distance downstream of the jet exit. On the other hand, the additional resolution provided by the present multiblock grid in the wake region yields results that capture much more adequately the expected flow features. Although results are not shown here, it should be further emphasized that convergence rates for the jet cases are again essentially unaffected by the multiblock implementation.

Concluding Remarks

The extension of an existing axisymmetric, flow simulation capability has been performed to allow the use of structured, multiblock grids. The implemented formulation includes viscous, turbulent flows over axisymmetric configurations. The original code offers a choice among three different eddy viscosity turbulence closure models, but only two of them, namely, the Baldwin and Lomax and the Baldwin and Barth models, have been tested with the multiblock implementation so far. The results with the Baldwin and Barth model provide better comparison with the available data, especially for the afterbody cases. The applications of major interest concern afterbody flows over the first Brazilian satellite launcher, the VLS.

The multiblock capability implementation was validated using flow simulations over the VLS forebody. Computational results for these cases were available from previous calculations using a single-block grid. There was no degradation in solution accuracy that could be attributed to the additional internal block boundaries present in the multiblock simulations. Property contours cross block boundaries in a completely seamless fashion. No oscillations or discontinuities in the contours could be observed in the forebody results run. Moreover, the use of multiblock grids has not degraded the convergence rate for these forebody simulations.

Afterbody simulations considered cases with and without a base jet. However, the major emphasis of the work was on the analysis of the afterbody cases without a propulsive jet. The results with the present code were compared with those obtained using the single-block code and with experimental data for general cylindrical afterbodies at zero angle of attack. In general, the multiblock results show a marked improvement in the resolution of flow features, as compared to the previous single-block solutions. Moreover, the computational results reproduce the trends observed in the experimental data in terms of the location of the rear stagnation point as a function of the Mach number. For subsonic freestream Mach number cases, the discrepancies between computational and experimental values for this parameter were at most of 10%. The quantitative agreement in the supersonic case was poorer, but again the correct trend was captured.

Computational results for the afterbody cases, both with and without the propulsive jet, calculated with the Badwin and Barth model indicated very good property contour continuity across block interfaces. Moreover, in the overall sense, the rate of convergence to steady state remained essentially unaltered with the introduction of the multiblock capability. Both the number of iterations for convergence and the level of maximum residue reduction are not significantly different from the cases computed with a single-block grid. On the other hand, the additional resolution of flow details provided by the multiblock grids are evident from the results presented.

Acknowledgments

The present work was partially supported by Conselho Nacional de Desenvolvimento Científico e Tecnológico (CNPq) under the Integrated Project Research Grants 530109/93-0 and 522413/96-0. The availability of computational resources at Centro Nacional de Supercomputação of the Universidade Federal do Rio Grande do Sul and at Núcleo de Atendimento em Computação de Alto Desempenho of the Instituto Alberto Luiz Coimbra de Pós-Graduação e Pesquisa de Engenharia of the Universidade Federal do Rio de Janeiro is also gratefully acknowledged.

References

[1] Azevedo, J. L. F., Menezes, J. C. L., and Fico, N. G. C. R., Jr., "An Assessment of Boundary Layer Properties for Transonic and Supersonic Flows over the VLS," *Proceedings of the AIAA 13th Applied Aerodynamics Conference*, Pt. 1, AIAA, Washington, DC, 1995, pp. 41–51.

[2] Azevedo, J. L. F., Menezes, J. C. L., and Fico, N. G. C. R., Jr., "Accurate Turbulent Calculations of Transonic Launch Vehicle Flows," *Proceedings of the AIAA 14th Applied Aerodynamics Conference*, Pt. 2, AIAA, Reston, VA, 1996, pp. 841–851.

[3] Nietubicz, C. J., Pulliam, T. H., and Steger, J. L., "Numerical Solution of the Azimuthal-Invariant Thin-Layer Navier–Stokes Equations," AIAA Paper 79-0010, Jan. 1979.

[4] Deiwert, G. S., "Supersonic Axisymmetric Flow over Boattails Containing a Centered Propulsive Jet," *AIAA Journal*, Vol. 22, No. 10, 1984, pp. 1358–1365.

[5] Zdravistch, F., and Azevedo, J. L. F., "Numerical Simulation of High Speed Flows over Complex Satellite Launchers," *Proceedings of the 3rd Brazilian Thermal Sciences Meeting*, Vol. 1, Associação Brasileira de Ciências Mecânicas, Itapema, SC, Brazil, 1990, pp. 233–238.

[6] Baldwin, B. S., and Lomax, H., "Thin Layer Approximation and Algebraic Model for Separated Turbulent Flows," AIAA Paper 78-257, Jan. 1978.

[7] Johnson, D. A., and King, L. S., "A Mathematically Simple Turbulence Closure Model for Attached and Separated Turbulent Boundary Layers," *AIAA Journal*, Vol. 23, No. 11, 1985, pp. 1684–1692.

[8] Baldwin, B. S., and Barth, T. J., "A One-Equation Turbulence Transport Model for High Reynolds Number Wall-Bounded Flows," NASA TM-102847, Aug. 1990.

[9] Beam, R. M., and Warming, R. F., "An Implicit Factored Scheme for the Compressible Navier–Stokes Equations," *AIAA Journal*, Vol. 16, No. 4, 1978, pp. 393–402.

[10] Pulliam, T. H., and Steger, J. L., "Implicit Finite Difference Simulations of Three-Dimensional Compressible Flow," *AIAA Journal*, Vol. 18, No. 2, 1980, pp. 159–167.

[11] Pulliam, T. H., "Artificial Dissipation Models for the Euler Equations," *AIAA Journal*, Vol. 24, No. 12, 1986, pp. 1931–1940.

[12] Azevedo, J. L. F., Moraes, P., Jr., Maliska, C. R., Marchi, C. H., and Silva, A. F. C., "Code Validation for High-Speed Flow Simulation over Satellite Launch Vehicle," *Journal of Spacecraft and Rockets*, Vol. 33, No. 1, 1996, pp. 15–21.

[13] Fernández, F. Z., "Simulação de Escoamentos Aerodinâmicos em Configurações Tipo Cluster" ("Simulation of Aerodynamic Flows over Cluster Type Configurations"), M.S. Dissertation, Dept. of Aeronautical Engineering, Inst. Tecnológico de Aeronáutica, São José dos Campos, SP, Brazil, Nov. 1990.

[14] Menezes, J. C. L., "Análise Numérica de Escoamentos Transônicos Turbulentos em Torno de Aerofólios" ("Numerical Analysis of Transonic Turbulent Flows About Airfoils"), M.S. Dissertation, Dept. of Aeronautical Engineering, Inst. Tecnológico de Aeronáutica, São José dos Campos, SP, Brazil, July 1994.

[15] Shirazi, S. A., and Truman, C. R., "A Study of Algebraic and Half-Equation Turbulence Models for Hypersonic PNS Predictions," AIAA Paper 88-0222, Jan. 1988.

[16] Azevedo, J. L. F., Fico, N. G. C. R., Jr., Ortega, M. A., and Luna, G. C., "Nozzle Flow Computations Using the Euler Equations," *Proceedings of the 18th Congress of the International Council of the Aeronautical Sciences*, Vol. 1, International Council of the Aeronautical Sciences, Washington, DC, 1992, pp. 97–107.

[17] Azevedo, J. L. F., Fico, N. G. C. R., Jr., and Ortega, M. A., "Two-Dimensional and Axisymmetric Nozzle Flow Computations Using the Euler Equations," *Journal of the Brazilian Society of Mechanical Sciences*, Vol. 17, No. 2, 1995, pp. 147–170.

[18] Gregório, E. L., "Simulação Numérica de Escoamentos em Regiões Traseiras de Veículos Lançadores" ("Numerical Simulation of Flows in the Afterbody Region of Launch Vehicles"), Graduation Project, Dept. of Aeronautical Engineering, Inst. Tecnológico de Aeronáutica, São José dos Campos, SP, Brazil, Nov. 1995.

[19] Fletcher, C. A. J., *Computational Techniques for Fluid Dynamics 2. Specific Techniques for Different Flow Categories*, Springer–Verlag, Berlin, 1988, pp. 101–109.

[20] Merz, R. A., Page, R. H., and Przirembel, C. E. G., "Subsonic Axisymmetric Near-Wake Studies," *AIAA Journal*, Vol. 16, No. 7, 1978, pp. 656–662.

[21] Herrin, J. L., and Dutton, J. C., "Supersonic Base Flow Experiments in the Wake of a Cylindrical Afterbody," *AIAA Journal*, Vol. 32, No. 1, 1994, pp. 77–83.

J. R. Maus
Associate Editor